NJC

ROYAL SOCIETY OF CHEMISTRY

PAPER

Published on 06 March 2025
Licence and permissions

Check for updates

Cite this: *New J. Chem.*, 2025, **49**, 5240

Towards an efficient delayed fluorescence mechanism from charge transfer and local transitions. The role of heavy halide atoms†

Macarena Rojas-Poblete, [a] Raúl Guajardo-Maturana, *[a] Plinio Cantero-López [b] and Alvaro Muñoz-Castro *[c]

Received 18th November 2024,
Accepted 21st February 2025

DOI: 10.1039/d4nj04975f

rsc.li/njc

Finding organic nanostructures exhibiting luminescent behavior is a relevant issue in the development of functional molecules. In this context, the possibility of incorporating them into the architecture of organic light-emitting diode (OLED) devices has been investigated to improve their efficiency and photophysical stability for predicting the suitability of the emissive material. Herein, we unraveled the excitation mechanism and the role of the coupling constant in an uncommon planar structure. Intersystem crossing (ISC) represents a necessary process, so understanding the rate constant allows assessment of the suitability of a material. We calculated the ISC and reverse rates for hexamethylazatriangulene-triazine HMAT-TRZ (**1a**) and its functionalization with an iodide-atoms counterpart HMAT-TRZ-I_2 (**1b**), thereby uncovering the role of the heavy atoms. Our results account for moderate singlet–triplet gaps, ΔE_{ST} (0.1–0.2 eV). Moreover, HMAT-TRZ-I_2 enhanced the spin–orbit parameter, which accounted for ISC rates at the μs scale, and thus improved their luminescent characteristics. Calculations were conducted using time-dependent density functional theory, with the PBE0-D3 level providing an accurate response for the large molecules studied herein.

Introduction

Emissive molecules have a wide range of applications in electronic devices and show impressive performance in organic light emitting diodes (OLEDs), semiconductors, and imaging photovoltaics.[1,2] The primary drawbacks of organic materials in OLEDs research have been largely addressed due to the tuning of organic dyes towards bulk nanostructure materials with ultrasmall singlet–triplet gaps (ΔE_{ST}) and a slight increase in spin–orbit coupling (SOC). Much attention has been focused on thermally activated delayed fluorescence (TADF) given its ability to harvest triplet excitons through reverse intersystem crossing (ISC), which can be upconverted to a singlet state followed by radiative $S_1 \rightarrow S_0$ decay, and such a situation is triggered by thermal conditions. In fact, TADF materials with smaller singlet–triplet gaps provide internal quantum efficiency (IQE) that surpasses conventional OLED emitters in creating efficient OLEDs devices.

Such TADF compounds are particularly important for creating innovative materials and also play a part in biomedical applications and nanotechnology applications.[3] TADF features are commonly observed in organic molecules but also in inorganic complexes, such as Cu(I) metal–ligand complexes[4–9] with negligible distortions among ground and excited states, which remove the vibrational losses and resulting in an enhanced response.[10–19]

In this regard, purely organic emitters yield significant findings related to electroluminescent issues by leveraging the reverse intersystem crossing (rISC) process. This approach modulates the characteristics of the emitters, resulting in low-cost and environmentally friendly materials. Thus, in "tailored" conjugated chromophores, the TADF mechanism is maximized *via* the electronic population of the first singlet excited state since the first triplet manifold. Complementary theoretical calculations include higher-lying triplet states (T_n) for evaluating the molecular orbitals and their relationship with other states. Such findings reveal the electronic path or hopping due to the interconversion of singlets to triplets, followed by triplet exciton up-conversion. These actions lead to delayed emission and contribute to nearly 100% quantum yields, which minimize nonradiative deactivations.[20,21] The small ΔE_{ST} ($\Delta E_{ST} = E(S_1) - E(T_1)$) generally takes place thanks to the spatial separation of wave functions in the highest occupied molecular orbitals (HOMOs) and lowest unoccupied

[a] *Universidad SEK, Facultad de Ciencias de la Salud, Instituto de Investigación Interdisciplinar en Ciencias Biomédicas SEK (I3CBSEK) Chile, Fernando Manterola 0789, Providencia, Santiago, Chile. E-mail: rhguajar@uc.cl*
[b] *Universidad Andres Bello, Facultad de Ciencias Exactas, Departamento de Ciencias Químicas, Viña del Mar 2531015, Chile*
[c] *Facultad de Ingeniería, Arquitectura y Diseño, Universidad San Sebastián, Bellavista 7, Santiago, 8420524, Chile. E-mail: alvaro.munozc@uss.cl*

† Electronic supplementary information (ESI) available. See DOI: https://doi.org/10.1039/d4nj04975f

 This journal is © The Royal Society of Chemistry and the Centre National de la Recherche Scientifique 2025

molecular orbitals (LUMOs) that can be achieved through the strategic design of organic arrays, where smaller molecules are assembled as a building block. Hence, for an HOMO–LUMO transition, the exchange energy almost vanishes, thereby decreasing the ΔE_{ST} (which is an essential parameter involved in TADF mechanisms). Such processes collect the prompt and delayed luminescence resulting from the exciton hopping between estates with different symmetries.[22–24] We conducted calculations of the overall parameters that take place in the TADF, starting from the ISC process (facilitating a smaller ΔE_{ST} to align with an increase in SOC). Then, we calculated the ISC rate constant k_{ISC} (which remains in the principal transition of the singlet and triplet states thanks to the SOC between the wave functions of the involved electronic states) and the rISC rate (k_{rISC}) using excited state dynamic approaches. Furthermore, the Marcus–Levich–Jortner theory was employed to calculate the reorganization energy (λ). The latter encompasses the structural and energy changes associated with the decay of the higher-lying singlet states into the first excited state (*i.e.*, the initial stage above the crossing dynamic).

In particular, the structure of hexamethylazatriangulene-triazine (HMAT-TRZ (**1a**))[25] presents a prototypical template for efficient TADF devices. It features a non-conventional twisted backbone and its rigid design enables it to be a TADF device. It grants functionalization with iodides and enables investigating of the heavy atom effect in planar structures. Recently, some studies have led to the inclusion of bromide in organic TADF emitters[26,27] with the aim of enhancing crossing rates due to the increased strength of SOC. This situation mainly focuses on improving the rISC process because faster ISC can benefit direct triplet decay. We selected iodides to observe a slight inductive substituent effect in the ring structure and to explore additional relativistic effects in free metal compounds.

We investigated an organic TADF emitter and its potential substitution with heavy iodine atoms (which increases SOC) to achieve improved performance for the TADF. Herein, we obtained an electronic structure with the aid of quantum chemical calculations exploring the emission path. We studied the involved states, giving information of the absorption, emission, ΔE_{ST} and coupling among states. Besides, imaging of natural transition orbitals (NTOs) provided hole–electron system densities.

Computational details

Density functional theory[28] calculations were conducted employing the ORCA 5.0.4 package.[29,30] We used the old-SVP basis for H atoms, old-TZVP basis set for C, N, and the particular DKH-old-TZVP basis for I atoms. The ground and excited state optimizations for S_0, S_1, T_1 and T_2 states were carried out employing DFT and TD-DFT mark[31–34] from PBE0, and CAM-B3LYP functionals,[35–38] exploring the hybrid, range-separated, functionals. The optimized states were confirmed *via* vibrational analysis, without non-negative frequencies. The Douglas–Kroll–Hess Hamiltonian (DKH) approach[39] allowed us to solve the energy equation incorporating scalar relativistic corrections for the overall states.

Computations were conducted to optimize the ground states, followed by TD-DFT to obtain S_1, S_2, T_1, and T_2.[40] Spectra were modeled using the conductor-like polarized continuum model (PCM).[41–43]

Calculations of NICS and NICSzz were carried out at the TZ2P basis set at the Perdew–Burke–Ernzerhof (PBE) functional,[44] including relativistic effects *via* the scalar ZORA Hamiltonian.[45]

Crossing rates

ISC occurs due to the inclusion of SOC effects. ISC rates between a given initial state i and a final state manifold f can be calculated using Fermi's golden rule:[46,47]

$$k(\omega)_{if} = \frac{2\pi}{\hbar}\left|\langle \Psi_f | \hat{H}_{SO} | \Psi_i \rangle\right|^2 \delta(E_i - E_f) \quad (1)$$

The ISC rate was calculated using the excited state dynamics (ESD) module from the ORCA package. This module employs the Hessians for singlet and triplet states and computes the Franck–Condon factors between all initial and final states at room temperature. Consequently, Fermi's golden rule[46,47] expresses the reverse intersystem crossing rate constant:

$$k_{rISC} = \frac{2\pi}{\hbar}|V_{SOC}|^2 \times \rho FCWD \quad (2)$$

where $|V_{SOC}|^2$ affords the attainment of the k_{rISC}, giving accounts for the coupling term of the matrix representation of $\hat{H}_{SOC}$. The hopping transition from T_1 toward the S_1, involves three distinct states for each possible value of the total angular momentum: $J = -1, 0, 1$. $|V_{SOC}|^2$ can be depicted as an average of the three spin–orbit coupling matrix elements (SOCME):

$$|V_{SOC}|^2 = \frac{1}{3}\langle S_1 | \hat{H}_{SOC} | T_1 \rangle^2 = \frac{1}{3}\sum_{J=-1,0,1} \langle S_1 | \hat{H}_{SOC} | T_1^J \rangle \langle S_1 | \hat{H}_{SOC} | T_1^{J*} \rangle \quad (3)$$

Another key factor in k_{rISC} expression is ρ_{FCWD} (Franck–Condon-weighted density of states), which outlines the thermo-kinetic barrier linked to this process.

$$\rho_{FCWD}^{MLJT} = \frac{1}{\sqrt{4\pi\lambda_M k_B T}} \times \sum_{n=0}^{\infty} \exp(-S_{eff})\frac{S_{eff}^n}{n!}\exp\left(-\frac{(\Delta E_{ST} + n\hbar\omega_{eff} + \lambda_M)^2}{4\pi\lambda_M k_B T}\right) \quad (4)$$

In this context, the semiclassical Marcus theory[48,49] (SCMT) connects the potential energy surfaces of both states using parabolic functions centered around their respective energy minima.

Results

HMAT-TRZ (**1a**) is a hyper-conjugated chromophore featuring a fully planar backbone in which two primary units are connected

(a rigid triangulene and diphenyl triazine) to form a bulky structure with exceptional luminescent properties. In addition to being a potential TADF for OLEDs devices, we assessed an iodine-decorated counterpart to facilitate a heavy metal effect. The calculated dihedral angles between HMAT and TRZ serve as a suitable parameter for evaluating structural deviations between both the ground and excited states. Results showed that the D(CCCN)-1 angle was 0.55°, 0.16° and −0.86° in S_0, S_1, and T_1 for HMAT-TRZ, respectively, and in HMAT-TRZ-I_2 (**1b**) the angle was −0.90°, 0.19° and 0.06°, respectively. These data helped us clarify a significant tendency to maintain a completely planar structure in the corresponding excited states and their potential substitutions. D(NCCC)-1 and D(NCCC)-2 are the dihedral angles between the phenyl and triazine, with values ranging from 0.99° to 0.07°, which also highlighted planar features that expanded in the overall structure. Table S1 (ESI†) summarizes the main angles and bond distances calculated for the current molecules, which align well with experimental data parameters. The spectroscopic properties of HMAT-TRZ and HMAT-TRZ-I_2 involve almost coplanar conformations at their related electronic states. Coplanar TADF emitters had slight extensions compared with those that show a twisted conformation because these reached smaller ΔE_{ST} values, and pure charge-transfer excitations. First, we modelled the absorption and fluorescent spectra (Fig. 1), which overall aligned with the experimental data. Thus, S_0 displayed characteristic peaks at approximately 425 nm and 438 nm for HMAT-TRZ and HMAT-TRZ-I_2 respectively, which are very close to the experimental value (420 nm). Furthermore, the dipole moment ascribed to the singlet state transition ($\mu_{s_1-s_0}$) corresponded to 5.5D and 5.7D, indicating a slight improvement for HMAT-TRZ-I_2, in addition to the assessed redshift of the corresponding peak. Furthermore, these transition dipole moments were small according to an earlier report.[25] Thus, $\mu_{s_1-s_0}$ yielded relatively small values due to the few overlaps present in HOMO–LUMO orbitals. In this sense, these values were not small enough to indicate a decrease in the luminescent character.

Studies have demonstrated that coplanar structures can also be efficient TADF emitters owing to the hindered non-radiative decay caused by the rigid backbone.[25,50–52] Thus, between ground state absorption and S_1 transitions a significant redshift occurs triggered by the change in the nature of orbital densities. The S_0 state gives way to local excitation, with $\pi \rightarrow n^*$ character, whereas S_1 generates charge-transfer excitations showing a clear $\pi \rightarrow \pi^*$ type (Fig. 3), and this situation remains in **1a**- and **1b**-substituted iodide arrays. One could argue that the S_1 signal stays similar in both compounds because those transitions obey the character of the hole–electron densities rather than a change in structural rearrangement for the incoming presence of iodide substituents, in addition to the structures remaining similar regardless of the electronic state calculated.

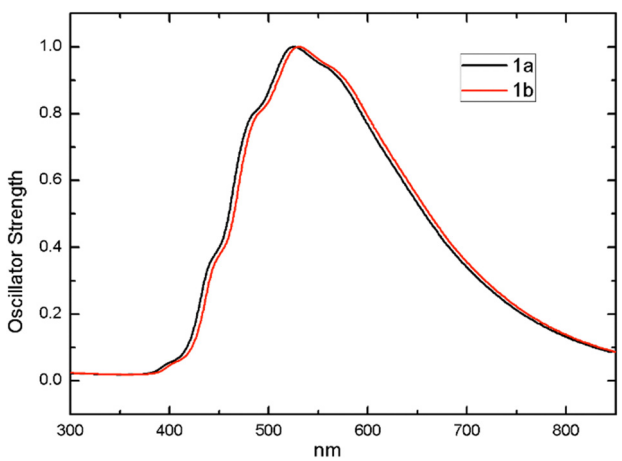


Fig. 1 Singlet emission spectra ($S_1 \rightarrow S_0$) for **1a** and **1b**. Calculated from the frequencies of singlet and ground states.

HMAT-TRZ was characterized as a potential TADF emitter. The transient photoluminescent decay spectra in doped films revealed delayed fluorescence up to 300 K[25] with some dependence on the host or film. These spectra provided an estimation of ΔE_{ST} of ∼0.38 eV. This value is not in the order of a typical TADF emitter. However, it may be been an overestimation because there were additional interactions in the doped film due to mixture with the host. Quantum calculations delivered a smaller value because the theoretical model was constructed with the main compound avoiding interactions with the host in the film. Furthermore, the TADF components typically showed values of ΔE_{ST} near or below 0.1 eV, indicating that larger values would barely display delayed emission.

Crossing rates

ISC rate. We calculated the spin-forbidden crossing rates for $S_1 \rightarrow T_1$ and $T_1 \rightarrow S_1$ transitions (Fig. 2). Such electronic hopping is often hard to observe upon experimentation. Hence, we took advantage of the theoretical results to give a deeper analysis of excited state dynamics. Additionally, we computed the manifold of higher-lying states such as T_1 and T_2. Thus, ISC can be regarded as the sum of the two electronics crossings. The T_n ($n = 3 \cdots n$) states of further energy levels reflect negligible values of the ISC rate.

The crossing between states occurs when excitons in higher states lose energy and fall to the first singlet S_1. Immediately, ISC occurs to T_1 or T_2, which can be quantified and summed to provide a reliable calculation. Fig. 3 shows the localized NTO for singlet and triplet transitions. According to the El-Sayed rules,[53,54] the ISC is relatively large if this radiationless transition involves a change of orbitals. For example, the $^1\pi, \pi^* \rightarrow {}^3n, \pi^*$ is faster than $^1\pi, \pi^* \rightarrow {}^3\pi, \pi^*$ transitions. The picture here reflects a clear $^1\pi, \pi^* \rightarrow {}^3\pi, n^*$ and, $^1\pi, \pi^* \rightarrow {}^3n, \pi^*$ for **1a** and **1b** compounds, instead of T_2 states, give $^1\pi, \pi^* \rightarrow {}^3\pi, \pi^*$ transitions. Such an observation provides insight into the corresponding analysis of the involved rates calculated here, confirming the suitability of the chromophores for TADF applications. Besides, the NTO hole–electron densities generate charge-transfer transitions in most cases, allowing a decrease in exchange energy and therefore of ΔE_{ST}. The molecular design generates the mentioned effect. Here, the aggregated moieties resembled "building block" synthesis. In this context, dynamic calculation of ISC rates was carried out using the triplet coordinates and Hessians for both singlet and triplet

 This journal is © The Royal Society of Chemistry and the Centre National de la Recherche Scientifique 2025

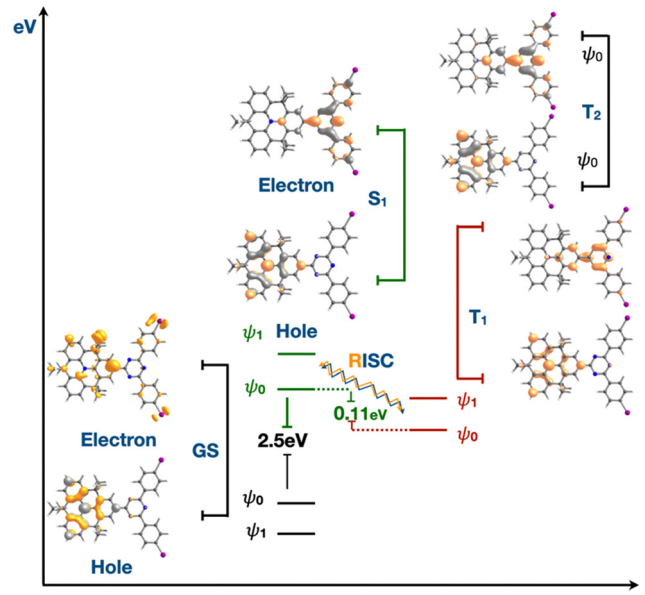


Fig. 2 Transition process for the related states in **1b**.

states in an accurate process whereby values were determined as the sum of $S_1 \rightarrow T_1$ and $S_1 \rightarrow T_2$ hopping. We collected both contributions to the final result amounting to 1.2×10^5 and 1.9×10^6 for **1a** and **1b**, respectively (Table 1). These quantities indicated the increase in crossing due to the heavy atom(ı) effect with higher coupling. Such values reached the order of other TADF emitters with a classical twisted structure.

The ΔE_{ST} gaps were 0.22 eV and 0.12 eV computed to the PBE0-D3 level, which is a proved theoretical level in organic TADFs. As reported by Kunze and coworkers,[55] the CAM-B3LYP functional generally underestimates ΔE_{ST} values.[56] Our result suggests that the electronic hopping occurring from triangulene → triazine moieties, whether in the ground or excited states of two compounds, only changed the type of orbital projection. We analyzed the time when the excitons in the triplet state could relax back to a singlet manifold whose pathway can either finish in a singlet decay or anew straight back to a triplet manifold. This route introduces some degree of cycling to TADF dynamics, enabling the process to continue without loss of electronic populations.

rISC rate. rISC is seen as electronic hopping going from the $T_1 \rightarrow S_1$ manifold. It is hard to observe such hopping because the triplet excitons can go back to the singlet at any time, which is regarded as a steady-state. Besides, the electronic population rarely can be in an appropriate relationship. One can calculate

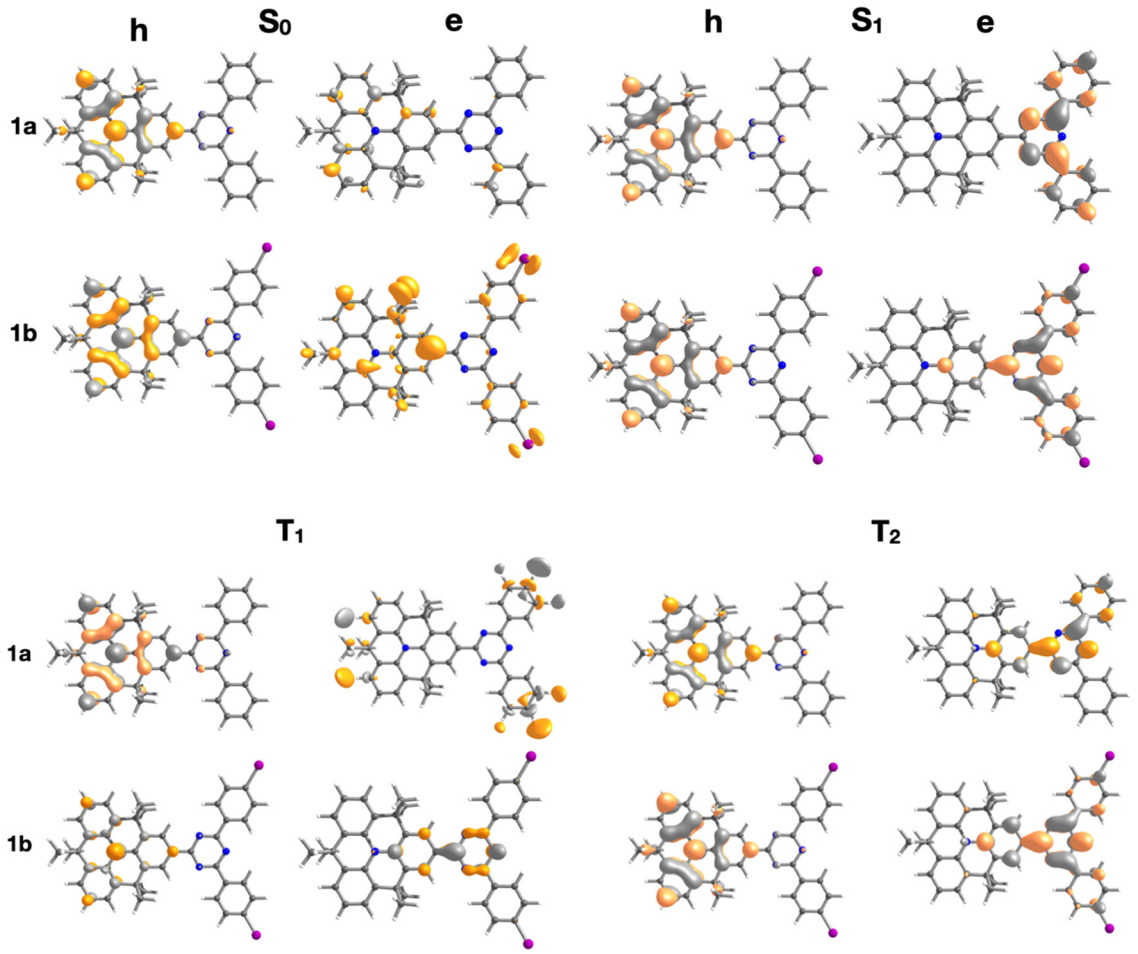


Fig. 3 Main orbitals iso-surface showing electronic path movement.

Table 1 Calculated absorption and emission transitions (oscillator strength (os), transition dipole moment (μ (D)), singlet–triplet gap ΔE_{ST} (eV), intersystem crossing rate k_{ISC} (s^{-1}), reverse intersystem crossing rate k_{rISC} (s^{-1}), spin–orbit coupling SOC (cm^{-1})) for the corresponding states

		PBE0	Exp. (λ_{Max})
S_0			
1a	λ_{max}	425.1	420
	Os/μ (D)	0.7/5.5	
1b	λ_{max} (nm)	438.0	
	Os/μ (D)	0.7/5.7	
S_1			
1a	λ_{max} (nm)	$466_{Tol.}$; $571_{(CH_2Cl_2)}$	$460_{Tol.}$; $545_{(CH_2Cl_2)}$
	Os	0.4	
1b	λ_{max} (nm)	519.3	
	Os	0.0	

	1a	**1b**
ΔE_{ST} (eV)	0.22	0.12
H_{SOC} (cm^{-1})	0.03	0.16
$^1k_{ISC}$ (s^{-1})	8.9×10^2	1.0×10^5
$^2k_{ISC}$ (s^{-1})	1.2×10^5	1.8×10^6
K_{ISC} (s^{-1})	1.2×10^5	1.9×10^6
k_{rISC} (s^{-1})	5.1×10^{-2} 2.6×10^4	2.6×10^4
λ_M (eV)	0.054	0.049
Huang–Rhys (S)	0.024	0.700
ω_{eff} (eV)	0.180	0.176

the K_{rISC} rate through a steep-to-steep strategy, according to Fermi's golden rule:[46,47]

$$k_{RISC} = \frac{2\pi}{\hbar}\rho_{FC}\left|\langle S_1|\hat{H}_{SOC}|T_1\rangle\right|^2 \quad (5)$$

Here, ρ_{FC} is the Franck–Condon density of states, and $\langle S_1|\hat{H}_{SOC}|T_1\rangle$ accounts for the matrix SOC elements of triplet and singlet interactions. ρ_{FC} is the equation of the extended Marcus–Levich–Jortner theory.[57]

The reorganization energy accounts for intramolecular low-frequency vibrations. It provides valuable insights for incorporating energy losses before crossing and ensures accurate applicability for the large molecules discussed here. We used the parameters SOC, ΔE_{ST}, and reorganization energy, which are essential to elucidate TADF dynamics. Consequently, larger SOCs in organic molecules ameliorate the rISC rate. Otherwise, smaller values (*i.e.*, >0.2) of ΔE_{ST} can increase the rate, and the more common values of λ_M, that range between 0.1 to 0.2 can enable efficient performance in TADF.[57]

The relaxed structures for ground and excited states were obtained with relativistic corrections necessary due to the presence of heavy iodide atoms. The rISC rate delivered values in the range of organic TADF emitters but with a noticeable increase thanks to the incoming link of iodine atoms in the backbone. This calculation aligned with the presence of the additional parameter because $T_1 \rightarrow S_1$ transition can be triggered for a meaningful overlap between initial and final state nuclear wave functions. Consequently, extension of the Marcus–Levich–Jortner equation included high-frequency normal modes, typically $\omega_i > 1000$ cm^{-1}. The Huang–Rhys factors (S_{eff}) of this effective mode and corresponding frequencies $\hbar\omega_{eff}$ were calculated.

The final result generated very small differences with the classical Marcus equation, meaning that the crossing was revealed on low frequencies or for the reorganization energy. λ_M is the energy gap between E_{S_1/S_1} and E_{S_1/T_1}:

$$\lambda_M = E_{S_1/T_1} - E_{S_1/S_1}$$

where E_{S_1/T_1} is the S_1 state energy at the T_1 state geometry, and E_{S_1/S_1} is the S_1 state energy at the S_1 state geometry. Those can be seen as the corresponding vertical transitions, depicting the vibrational relaxations that occur upon the involved electronic transition. Thus, the values for **1a** and **1b** were 0.054 and 0.049 eV, respectively. These small values are in agreement with large very rigid structures with steric hindrance, and are slightly smaller than for other dyes studied for our research team.[58] In this context, k_{rISC} was 5.1×10^{-2} s^{-1} and 2.6×10^4 s^{-1} for **1a** and **1b**, respectively. The negligible quantity in **1a** was because the calculated ΔE_{ST} was greater than that for conventional organic TADF. However, functionalization from iodide atoms reached the value for a commonly utilized TADF emitter. This is an important result for planar organic structures with regard to OLEDs.

Additionally, Bergmann and co-workers,[59] contrary to previous assumptions, demonstrated that intramolecular hydrogen bonding does not significantly hinder dihedral rotation between donor and acceptor moieties. They established that the differences in photophysical properties among coplanar emitters result from variations in electronic structures rather than from hydrogen bonding effects.[60,61] Accordingly, we undertook the potential energy surface (PES) calculations shown in Fig. 4, focusing on rotation of dihedral angle D1 (specified in Fig. S1, ESI†) to identify the intersection of excited states (which aids in clarifying the angle related to each electronic crossing). As illustrated in the graph, HMAT-TRZ-I_2 had a singlet–singlet charge transfer between S_1 and S_2 around 70°. Along this line, the singlet–triplet crossing could occur ~10° among S_2 and T_1 or T_2 states. Both components of ISC

 This journal is © The Royal Society of Chemistry and the Centre National de la Recherche Scientifique 2025

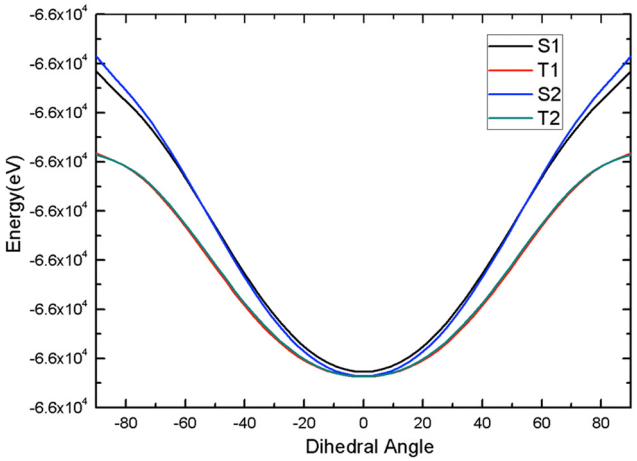


Fig. 4 PES for the singlet (S_1, S_2) and triplet (T_1, T_2) excited states in HMAT-TRZ-I_2, illustrating electronic crossing in the intersection curve.

$^1k_{ISC}$ and $^2k_{ISC}$ were significant, and so the results were summed (Table 1).

Aromaticity. To evaluate the aromatic properties in the overall HMAT-TRZ and HMAT-TRZ-I_2 structures, the induced magnetic field was calculated to account for NICS and B_z^{ind}, also noted as $NICS_{zz}$ (Fig. 5). For the NICS isosurface for HMAT-TRZ, the terminal phenyl rings (ring A) and fused rings exhibited larger shielding regions (ascribed as the most aromatic rings within the structure), followed by ring C, whereas rings B, D, and F remained as antiaromatic rings. The NICS value calculated at the center of each ring was −5.9, +2.1, −4.5, +4.7, −6.3, and, +4.5 ppm, respectively, for rings A, B, C, D, E, and F. The contour plot representation of NICS supported the aromatic character of some phenyl rings, separated by antiaromatic rings. Under a field oriented from the *z*-axis, the aromatic character of rings A, C, and E was denoted with $NICS_{zz}$ values at the center of each ring of −7.7, −5.6, and −5.7 ppm, respectively, and with $NICS_{zz}$ values of +18.6, +37.6, and, +37.0 ppm for the antiaromatic rings given by B, D, and, F, respectively.

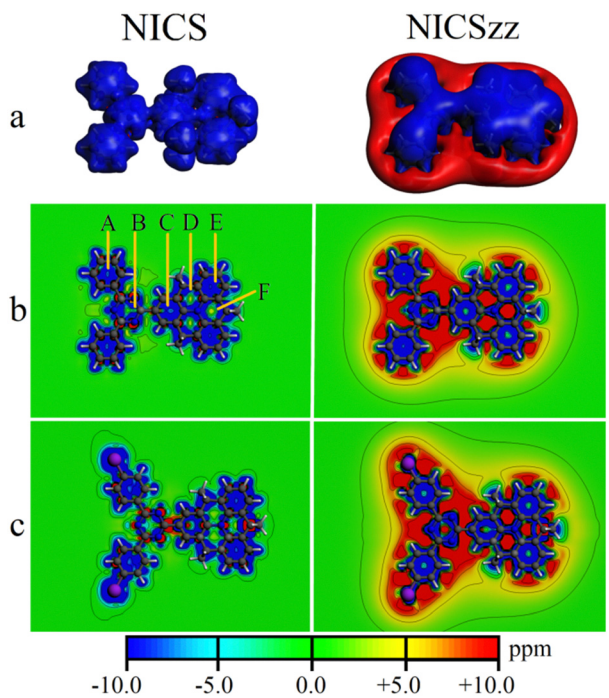


Fig. 5 Isosurface representation of NICS and $NICS_{zz}$ for SQ (a), and the respective contour plots for HMAT-TRZ (b) and HMAT-TRZ-I_2 (c). Isosurface value set at ±3.0 ppm.

Table 2 Calculated values of NICS and NICSzz at the center of each ring (ppm)

1a	NICS	$NICS_{zz}$	1b	NICS	$NICS_{zz}$
A	−5.9	−7.7	A	−4.9	−4.2
B	+2.1	+18.6	B	+2.1	+19.1
C	−4.5	−5.6	C	−4.5	−5.9
D	+4.7	+37.6	D	+4.7	+37.7
E	−6.3	−5.7	E	−6.3	−5.7
F	+4.5	+37.0	F	+4.5	+37.0

In addition, a continuous deshielding region of +3.0 ppm was denoted along with the contour of the structural backbone of HMAT-TRZ. For the iodine-decorated counterpart HMAT-TRZ-I_2, similar characteristics were found. The I-phenyl rings exhibited a decrease in central shielding values, as given by NICS, to −4.9 ppm, in comparison with HMAT-TRZ (Table 2).

Conclusions

From a study by Chen and co-workers, we modelled HMAT-TRZ and a heavy-atom iodide counterpart to shed light on the excited states dynamic mechanism to evaluate their potential application as a TADF device. Based on relevant calculations at ground and excited states, the ΔE_{ST} gap was obtained, and the role of iodine atoms evaluated. The charge reorganization upon electronic transitions, ISC, geometrical reorganization energy, and transition rates for S → T and T → S crossing revealed a $^1\pi$, $\pi^* \rightarrow {}^3\pi$, n* character, which is in line with the El-Sayed rule.

ISC is a dynamic process that is challenging to unravel. However, theoretical assessment provides essential information for evaluating the design of compounds intended for inclusion in OLEDs devices. The calculated ISC rates were consistent with those obtained for representative organic structures exhibiting efficient TADF features, as detailed in previous studies. k_{ISC} increased to microseconds in HMAT-TRZ-I_2, which could enhance the ISC, aiding the conversion between singlet and triplet states. On the other hand, the increase in rISC from 5.1×10^{-2} s^{-1} to 2.6×10^4 s^{-1} is desired for the conversion of T → S. Besides, an order of 10^4 for such a rate hardly would accelerate to a level in which undesired TADF phenomena occur.

Comparison with a system with two halide atoms accounted for higher SOC with faster ISC and rISC rates, enhancing its performance in emissive devices. This calculation used an extension of the Marcus–Levich–Jortner equation without noticeable differences with the Marcus equation. The electronic conjugation was not a restriction for rotation of the dihedral angle D1 because the $NICS_{zz}$ value of triazine indicated a lack of aromaticity character.

Author contributions

P. C.-L: investigation, methodology, and conceptualization. M. R.-P: methodology, data curation, and manuscript writing; R. G.-M and A. M.-C: supervision, conceptualization, and writing (original draft, review and editing).

Data availability

The data featured in this article are accessible in the ESI.†

Conflicts of interest

The authors have no conflicts of interest to disclose.

Acknowledgements

A. M.-C. is thankful for support from ANID FONDECYT Regular 1221676. This research was partially supported by the supercomputing infrastructure of the NLHPC (CCSS210001).

References

1 G. Li, Z. Q. Zhu, Q. Chen and J. Li, *Org. Electron.*, 2019, **69**, 135–152.
2 C. Bizzarri, E. Spuling, D. M. Knoll, D. Volz and S. Bräse, *Coord. Chem. Rev.*, 2018, **373**, 49–82.
3 A. Monkman, *Highly Efficient OLEDs: Materials Based on Thermally Activated Delayed Fluorescence*, 2018, pp. 425–463.
4 L. Maini, D. Braga, P. P. Mazzeo and B. Ventura, *Dalton Trans.*, 2012, **41**, 531–539.
5 A. Tsuboyama, K. Kuge, M. Furugori, S. Okada, M. Hoshino and K. Ueno, *Inorg. Chem.*, 2007, **46**, 1992–2001.
6 V. Pawlowski, G. Knör, C. Lennartz and A. Vogler, *Eur. J. Inorg. Chem.*, 2005, 3167–3171.
7 M. Nishikawa, K. Nomoto, S. Kume, K. Inoue, M. Sakai, M. Fujii and H. Nishihara, *J. Am. Chem. Soc.*, 2010, **132**, 9579–9581.
8 J. R. Kirchhoff, R. E. Gamache, M. W. Blaskie, A. A. Del Paggio, R. K. Lengel and D. R. McMillin, *Inorg. Chem.*, 1983, **22**, 2380–2384.
9 X.-F. Song, Z.-W. Li, W.-K. Chen, Y.-J. Gao and G. Cui, *Inorg. Chem.*, 2022, **61**, 7673–7681.
10 T. Gneuß, M. J. Leitl, L. H. Finger, N. Rau, H. Yersin and J. Sundermeyer, *Dalton Trans.*, 2015, **44**, 8506–8520.
11 J.-L. Chen, X.-F. Cao, J.-Y. Wang, L.-H. He, Z.-Y. Liu, H.-R. Wen and Z.-N. Chen, *Inorg. Chem.*, 2013, **52**, 9727–9740.
12 C.-W. Hsu, C.-C. Lin, M.-W. Chung, Y. Chi, G.-H. Lee, P.-T. Chou, C.-H. Chang and P.-Y. Chen, *J. Am. Chem. Soc.*, 2011, **133**, 12085–12099.
13 L. Bergmann, J. Friedrichs, M. Mydlak, T. Baumann, M. Nieger and S. Bräse, *Chem. Commun.*, 2013, **49**, 6501–6503.
14 A. J. M. Miller, J. L. Dempsey and J. C. Peters, *Inorg. Chem.*, 2007, **46**, 7244–7246.
15 S. Igawa, M. Hashimoto, I. Kawata, M. Yashima, M. Hoshino and M. Osawa, *J. Mater. Chem. C*, 2013, **1**, 542–551.
16 Z. Liu, P. I. Djurovich, M. T. Whited and M. E. Thompson, *Inorg. Chem.*, 2012, **51**, 230–236.
17 M. J. Leitl, F.-R. Küchle, H. A. Mayer, L. Wesemann and H. Yersin, *J. Phys. Chem. A*, 2013, **117**, 11823–11836.
18 D. M. Zink, T. Baumann, J. Friedrichs, M. Nieger and S. Bräse, *Inorg. Chem.*, 2013, **52**, 13509–13520.
19 J. C. Deaton, S. C. Switalski, D. Y. Kondakov, R. H. Young, T. D. Pawlik, D. J. Giesen, S. B. Harkins, A. J. M. Miller, S. F. Mickenberg and J. C. Peters, *J. Am. Chem. Soc.*, 2010, **132**, 9499–9508.
20 D. Di, A. S. Romanov, L. Yang, J. M. Richter, J. P. H. Rivett, S. Jones, T. H. Thomas, M. Abdi Jalebi, R. H. Friend, M. Linnolahti, M. Bochmann and D. Credgington, *Science*, 2017, **356**, 159–163.
21 S. Hirata, Y. Sakai, K. Masui, H. Tanaka, S. Y. Lee, H. Nomura, N. Nakamura, M. Yasumatsu, H. Nakanotani, Q. Zhang, K. Shizu, H. Miyazaki and C. Adachi, *Nat. Mater.*, 2015, **14**, 330–336.
22 Z. Yang, Z. Mao, Z. Xie, Y. Zhang, S. Liu, J. Zhao, J. Xu, Z. Chi and M. P. Aldred, *Chem. Soc. Rev.*, 2017, **46**, 915–1016.
23 H. Sun, Z. Hu, C. Zhong, X. Chen, Z. Sun and J.-L. Brédas, *J. Phys. Chem. Lett.*, 2017, **8**, 2393–2398.
24 F. B. Dias, K. N. Bourdakos, V. Jankus, K. C. Moss, K. T. Kamtekar, V. Bhalla, J. Santos, M. R. Bryce and A. P. Monkman, *Adv. Mater.*, 2013, **25**, 3707–3714.
25 X. Chen, Y. Tsuchiya, Y. Ishikawa, C. Zhong, C. Adachi and J. Brédas, *Adv. Mater.*, 2017, **29**, 1702767.
26 M. Mońka, I. E. Serdiuk, K. Kozakiewicz, E. Hoffman, J. Szumilas, A. Kubicki, S. Y. Park and P. Bojarski, *J. Mater. Chem. C Mater*, 2022, **10**, 7925–7934.
27 M. Mońka, S. Gogoc, K. Kozakiewicz, V. Ievtukhov, D. Grzywacz, O. Ciupak, A. Kubicki, P. Bojarski, P. Data and I. E. Serdiuk, *ACS Appl. Mater. Interfaces*, 2024, **16**, 15107–15120.
28 K. G. Dyall and K. Fægri, *Introduction to relativistic quantum chemistry*, Oxford University Press, 2007.
29 F. Neese, *WIREs Comput. Mol. Sci.*, 2022, **12**, e1606.
30 F. Neese, *WIREs Comput. Mol. Sci.*, 2012, **2**, 73–78.
31 E. Van Lenthe, J. G. Snijders and E. J. Baerends, *J. Chem. Phys.*, 1996, **105**, 6505–6516.
32 S. J. A. van Gisbergen, J. G. Snijders and E. J. Baerends, *Comput. Phys. Commun.*, 1999, **118**, 119–138.
33 A. Rosa, E. J. Baerends, S. J. A. van Gisbergen, E. van Lenthe, J. A. Groeneveld and J. G. Snijders, *J. Am. Chem. Soc.*, 1999, **121**, 10356–10365.
34 F. Wang, T. Ziegler, E. van Lenthe, S. van Gisbergen and E. J. Baerends, *J. Chem. Phys.*, 2005, **122**, 204103.
35 A. D. Becke, *Phys. Rev. A*, 1988, **38**, 3098–3100.
36 C. Lee, W. Yang and R. G. Parr, *Phys. Rev. B: Condens. Matter Mater. Phys.*, 1988, **37**, 785–789.
37 S. H. Vosko, L. Wilk and M. Nusair, *Can. J. Phys.*, 1980, **58**, 1200–1211.
38 T. Yanai, D. P. Tew and N. C. Handy, *Chem. Phys. Lett.*, 2004, **393**, 51–57.

 This journal is © The Royal Society of Chemistry and the Centre National de la Recherche Scientifique 2025

39 B. Sandhoefer, S. Kossmann and F. Neese, *J. Chem. Phys.*, 2013, **138**, 104102.
40 P. Cantero-López, L. Le Bras, D. Páez-Hernández and R. Arratia-Pérez, *Dalton Trans.*, 2015, **44**, 20004–20010.
41 S. Miertuš and J. Tomasi, *Chem. Phys.*, 1982, **65**, 239–245.
42 S. Miertuš, E. Scrocco and J. Tomasi, *Chem. Phys.*, 1981, **55**, 117–129.
43 J. L. Pascual-ahuir, E. Silla and I. Tuñon, *J. Comput. Chem.*, 1994, **15**, 1127–1138.
44 J. P. Perdew, K. Burke and M. Ernzerhof, *Phys. Rev. Lett.*, 1996, **77**, 3865–3868.
45 E. van Lenthe, J. G. Snijders and E. J. Baerends, *J. Chem. Phys.*, 1996, **105**, 6505–6516.
46 G. W. Robinson and R. P. Frosch, *J. Chem. Phys.*, 1963, **38**, 1187–1203.
47 V. Lawetz, G. Orlandi and W. Siebrand, *J. Chem. Phys.*, 1972, **56**, 4058–4072.
48 G. L. Closs, L. T. Calcaterra, N. J. Green, K. W. Penfield and J. R. Miller, *J. Phys. Chem.*, 1986, **90**, 3673–3683.
49 R. A. Marcus, *Annu. Rev. Phys. Chem.*, 1964, **15**, 155–196.
50 Z. Fang, V. Chellappan, R. D. Webster, L. Ke, T. Zhang, B. Liu and Y.-H. Lai, *J. Mater. Chem.*, 2012, **22**, 15397.
51 Z. Fang, X. Zhang, Y. Hing Lai and B. Liu, *Chem. Commun.*, 2009, 920–922.
52 S. A. Elgadi, D. M. Mayder, R. Hojo and Z. M. Hudson, *Adv. Opt. Mater.*, 2023, **11**, 2202754.
53 In The IUPAC Compendium of Chemical Terminology, International Union of Pure and Applied Chemistry (IUPAC), Research Triangle Park, NC, 2014.
54 M. A. El-Sayed and L. Hall, *J. Chem. Phys.*, 1969, **50**, 3113–3114.
55 L. Kunze, A. Hansen, S. Grimme and J.-M. Mewes, *J. Phys. Chem. Lett.*, 2021, **12**, 8470–8480.
56 F. Claveria-Cadiz, M. Rojas-Poblete, A. Muñoz-Castro, E. Schott and R. Guajardo-Maturana, *J. Photochem. Photobiol., A*, 2024, **452**, 115547.
57 Y. Olivier, B. Yurash, L. Muccioli, G. D'Avino, O. Mikhnenko, J. C. Sancho-García, C. Adachi, T. Q. Nguyen and D. Beljonne, *Phys. Rev. Mater.*, 2017, **1**, 075602.
58 F. Claveria-Cadiz, M. Rojas-Poblete, A. Muñoz-Castro, E. Schott and R. Guajardo-Maturana, *J. Photochem. Photobiol., A*, 2024, **452**, 115547.
59 K. Bergmann, R. Hojo and Z. M. Hudson, *J. Phys. Chem. Lett.*, 2023, **14**, 310–317.
60 M. Hempe, N. A. Kukhta, A. Danos, A. S. Batsanov, A. P. Monkman and M. R. Bryce, *J. Phys. Chem. Lett.*, 2022, **13**, 8221–8227.
61 S. Kuila, H. Miranda-Salinas, J. Eng, C. Li, M. R. Bryce, T. J. Penfold and A. P. Monkman, *Nat. Commun.*, 2024, **15**, 9611.